

Dose and image quality for a cone-beam C-arm CT system

Rebecca Fahrig, Robert Dixon, Thomas Payne, Richard L. Morin, Arundhuti Ganguly, and Norbert Strobel

Radiology, Stanford University, Lucas MRS Imaging Center, 1201 Welch Rd., Rm. P-286, Palo Alto, California 94305

(Received 8 April 2006; revised 23 August 2006; accepted for publication 28 September 2006; published 16 November 2006)

We assess dose and image quality of a state-of-the-art angiographic C-arm system (Axiom Artis dTA, Siemens Medical Solutions, Forchheim, Germany) for three-dimensional neuro-imaging at various dose levels and tube voltages and an associated measurement method. Unlike conventional CT, the beam length covers the entire phantom, hence, the concept of computed tomography dose index (CTDI) is not the metric of choice, and one can revert to conventional dosimetry methods by directly measuring the dose at various points using a small ion chamber. This method allows us to define and compute a new dose metric that is appropriate for a direct comparison with the familiar $CTDI_w$ of conventional CT. A perception study involving the CATPHAN 600 indicates that one can expect to see at least the 9 mm inset with 0.5% nominal contrast at the recommended head-scan dose (60 mGy) when using tube voltages ranging from 70 kVp to 125 kVp. When analyzing the impact of tube voltage on image quality at a fixed dose, we found that lower tube voltages gave improved low contrast detectability for small-diameter objects. The relationships between kVp, image noise, dose, and contrast perception are discussed. © 2006 American Association of Physicists in Medicine. [DOI: 10.1118/1.2370508]

Key words: C-arm CT, cone-beam computed tomography, dose, image quality

I. INTRODUCTION

Cone-beam C-arm imaging has entered clinical routine for neuro-interventional applications permitting the visualization of detailed cerebral vasculature.¹⁻³ With new improvements in detector technology, image reconstruction, and image correction algorithms,⁴⁻⁸ three-dimensional (3D) cone-beam C-arm imaging is now beginning to be used for low-contrast imaging applications such as detection of fresh intracranial bleeds.⁹ This new imaging modality must therefore be evaluated so that the trade-offs between patient dose and image quality is understood.

To achieve improved low-contrast imaging performance, many single C-arm projections are required, thus creating a need to ensure that the trade-off between image quality and patient dose is well characterized and understood. The incident energy impinging on the patient from C-arm devices has traditionally been based on “in-air” dose-area-product measurement devices¹⁰⁻¹³ from which energy imparted may be calculated (or even entrance dose or ESE using the area of the collimator aperture). For conventional CT imaging, the computed tomography dose index (CTDI), which represents a dose inside a standard phantom, has been used.

Since the beam coverage of volumetric imaging devices in the z direction has increased significantly, traditional CT dose metrics such as CTDI and measurement techniques designed for narrow collimations such as the 100 mm long pencil chamber are no longer applicable. In a recent report on a full-scale simulation model, Kroon defined a “rotational x-ray dose index” (RXDI) for dose measurements using the related CTDI phantoms as starting points and introduced the “weighted RXDI” ($RXDI_w$) defined by analogy to the famil-

iar weighted conventional CT dose index ($CTDI_w$).¹⁴ However, Kroon did not elaborate on how RXDI and ($RXDI_w$) should be measured. They cannot properly be measured using the 100 mm pencil chamber methodology of conventional CT. We had independently arrived at the same dose metric as the logical analogue to conventional CT doses and also demonstrated a measurement technique using a conventional ion chamber.¹⁵

Dixon has previously suggested the use of a small ion chamber to obtain a direct measurement of the accumulated dose in the central scan plane resulting from a helical or axial scan series for conventional narrow beam CT,¹⁶ and Anderson *et al.* proposed a dosimetry schema for 3D angiography systems using Dixon’s short ion chamber approach using the CT head phantom.¹⁷ Metrics^{16,17} based on averaging the dose over an arbitrary axial length of 10 cm (based on the length of a commonly used pencil chamber) do not represent the analog of the CTDI and are not considered appropriate, as discussed later.

For evaluation of low-contrast (LC) imaging performance of CT-like devices, objective and subjective methods are available. Since it is still very common to state the LC performance of a CT imaging system via the visibility of single objects, we opted for an observer-based subjective image quality study involving an image quality phantom.¹⁸ While a ROC analysis could be used to determine the visibility of small-sized objects under certain imaging conditions, a more time-efficient approach has been proposed by Ishida *et al.* in which they express the likelihood of detection as a function of target size and scan conditions using detectability profiles.¹⁹

The goal of this paper is to show how low contrast detectability of a 3D C-arm CT device can be experimentally evaluated under different imaging conditions and to provide benchmark results for a typical (“neuro”) system at standard dose levels. To this end, we first propose a dose metric and review an associated measurement method. We then analyze image quality based on perception experiments involving detectability profiles. We also compare C-arm CT imaging performance at various tube voltages, detector input dose settings, and patient dose levels, and compare this performance to conventional CT at comparable dose levels.

II. METHODS AND MATERIALS

This paper reports primarily on dose and image quality measurements performed using a state-of-the-art C-arm CT device. To characterize image quality differences at different dose levels, we derive a relationship between just visible object diameter and dose. This relationship also provides the ability to compare image quality across different tube voltages at a selected reference dose.

A. Dose metric and measurements

Since image quality evaluation is directly related to the radiation dose required to produce an image, radiation dose determination and dose metric for C-arm CT are discussed at the outset. For conventional CT, the dose metric $CTDI_{100}$ is used to estimate the average accumulated dose delivered by a scan series of length L in the central plane of the phantom at the center of the scan length $z=0$. For helical scans, it has been shown^{19,20} that $CTDI_{100}$ represents the angular average dose at $z=0$ for a scan length of $L=100$ mm. [If (r, θ) locates a given longitudinal z axis relative to the axis of rotation (AOR), the angular average is over all such axes ($-\pi \leq \theta \leq \pi$) at a fixed radius r (in a ring around the AOR) at the fixed value of $z=0$.] For axial scans; $CTDI_{100}$ is equal to the average accumulated dose (MSAD²¹) at the center of the scan length $z=0$ for a scan length of $L=100$ mm, and it is *not* a z -average dose over any appreciable part of the scan length L (and certainly not over ± 50 mm—even though its value is commonly indirectly inferred using a 100 mm long pencil chamber).

In C-Arm CT where the extent of the beam along the (z) axis of rotation may be up to 30 cm, the CTDI concept is no longer useful and measurement logically reverts to conventional dosimetry. That is, the radiation dose in the central phantom plane ($z=0$) can be measured using a small volume ion chamber inserted into an axial hole in the standard CT dosimetry phantoms such as the 16 cm diameter Perspex® head phantom used in this study. The ubiquitous 0.6 cc Farmer ion chamber is found to be convenient for this purpose. This dose is therefore directly comparable to the MSAD or helical dose in conventional (narrow beam) CT on that axis derived using CTDI. The Perspex CT dosimetry HEAD phantom should be roughly comparable in x-ray transmission to a 20 cm diameter unit density CATPHAN phantom used for image quality determinations based on mass density considerations (16 cm of Perspex with a den-

sity of 1.2 gm/cc is approximately equivalent to 19 cm of unit density material). The attenuation is in fact comparable at 125 kVp; however, differences in μ/ρ result in somewhat larger variation in mAs demand for the lower energy spectra generated at 70–80 kVp.

It is not appropriate to use a 100 mm pencil chamber to measure C-Arm CT doses, since it is designed for narrow beam, “single axial slice” dose integral measurements, and not for conventional “point” dosimetry which requires a short sampling length. Such a pencil chamber in a wide (>10 cm) beam would measure the average dose over an arbitrary length of 100 mm, which is not the analog of $CTDI_{100}$, $CTDI_W$, or MSAD of conventional CT, these being doses at the center of the scan length $z=0$. Moreover, the pencil chamber does not exhibit the flexibility required for “cone-beam” CT systems that can have variable beam widths both larger and smaller than 10 cm, at which point the meaning of the 100 mm pencil chamber reading changes from a value useful for predicting the accumulated dose for multiple contiguous scans to a dose average over an arbitrary 100 mm length.

A conventional CT scan series and C-arm CT both produce a similar dose distribution having a broad maximum at $z=0$, which maximum dose is represented by the existing $CTDI_{100}$ and related $CTDI_W$ metric as well as by our proposed metric. Our proposed metric does not require specification of the ion chamber, and measurement of “point” doses is robust and provides complete flexibility.

1. Proposed dose metric for C-arm and wide cone beam CT

Unlike conventional CT for which a 360° rotation produces a cylindrically symmetric phantom dose, today’s C-arm devices typically use a 210° rotation ($180^\circ + \text{fan angle}$), producing a nonuniform dose distribution $D(r, \theta, z)$ with the peak dose occurring in the central plane ($z=0$) on the side of the phantom closest to the focal spot, near the midpoint of the rotation angle θ (depending on the heel effect direction). We therefore will define the dose metric $\bar{D}(0)$ as the average dose over the central phantom plane at $z=0$, and we will adopt, for convenience, the same area-averaging approximation used in conventional CT called $CTDI_W$ in which the central axis dose D_0 ($r=0$) is weighted by 1/3 and peripheral axes doses $D_p(\theta)$ ($r=R-1$ cm, where R is the phantom radius) are weighted by 2/3, also independently suggested by Kroon.¹⁴ This is also the same calculation procedure for $CTDI_W$ that would be used for a conventional CT scanner using a rotation angle smaller than 360°. It should be noted that pitch has no relevance for C-arm CT.

In other words, the average dose over the central phantom plane at $z=0$ is defined as

$$\bar{D}(0) = (1/3)D_0 + (2/3)\bar{D}_p. \quad (1)$$

This dose can be compared to $CTDI_W$ in conventional CT, assuming that Eq. (1) refers to $\bar{D}(0)$ based on doses measured in the standard “CTDI” dosimetry phantoms.



FIG. 1. Image acquisition setup. The CATPHAN 600 was aligned with the rotation axis (z axis) of the C-arm system. The phantom was positioned such that the midplane intersected the CTP515 soft-tissue module shown in Fig. 1.

2. Dose measurement

All dose values herein represent in-phantom doses in units of air kerma (f -factor=0.876). The dose was measured in the phantom midplane at the isocenter and also at eight peripheral positions in the 16 cm Perspex® dosimetry phantom at 1 cm depth from the surface. The C-arm was placed head-side and rotated around its “propeller axis” coincident with the couch z axis, as illustrated in Fig. 1, such that the gantry rotation and x-ray tube axes were parallel, resulting in the heel effect occurring in the z direction. A CNMC K602 Precision Electrometer and a Nuclear Enterprise 2571 (0.6 cc) Farmer chamber were used for the dose measurements made at four detector signal levels, “low,” “low-medium,” “medium-high,” and “high.” The ion chamber has been calibrated at an accredited dosimetry calibration laboratory and demonstrates a flat response (within 1.5%) over a range of HVL from 2 to 15 mm Al. The response of the automatic exposure control system (AEC) to the presence of the Farmer chamber was compared to AEC with the that of a standard 10 cm pencil chamber. The mAs per scan was found to be identical within measurement error for both measurement chambers, indicating that the metal of the Farmer chamber did not significantly perturb the system.

We also recorded the system-provided detector input exposure and the total mAs delivered during each C-arm image acquisition run, acquired over 20 s yielding 543 projections. Note that factory calibration establishes a known relationship between detector signal at a given kVp and detector exposure (measured before the grid) in nGy, which is recorded in the header of each projection image, and is referred to as detec-

TABLE I. Measured half-value layers at the operational kVps.

kVp	70	81	109	125
HVL (mm Al)	2.9	3.2	3.4	4.4

tor entrance dose hereafter. In addition, we monitored the tube voltage, since it may be increased by the automatic exposure control if the system cannot reach a desired detector entrance dose. Finally, the beam quality of the system was determined by measuring the half-value layer at the four operational voltages (70, 81, 109, and 125 kVp), as shown in Table I.

Note that our implementation of C-arm CT does not utilize a “bow-tie” filter, and the quality of the beam shown in Table I is “softer” than that of a conventional CT beam (about 7 mm Al at 120 kVp).

B. Image quality assessment

For 3D C-arm imaging, an Axiom Artis dTA (VB22D) C-arm system (Siemens Medical Solutions, Forchheim, Germany) with a 30 cm \times 40 cm flat-panel detector was used. The flat panel uses a CsI converter, with a thickness of approximately 200 g/cm².²⁰ Two approaches were taken to assess image quality of the imaging system: observer studies using low-contrast phantom images, and MTF measurements of a 100 μ m diameter steel wire under tension in air.

The image quality phantom for this evaluation was the 20 cm diameter CATPHAN 600 (Phantom Laboratories, New York). It was always aligned with the C-arm axis of rotation (z axis), and placed such that the scanner midplane intersected the CTP515 low-contrast CATPHAN module displayed in Fig. 2. The outer 40 mm long objects with various diameters (i.e., 2, 3, 4, 5, 6, 7, 8, 9, and 15 mm) were chosen for the study. The study was also restricted to objects with a nominal contrast of 0.5% to their surroundings.

With the C-arm in head-side position as shown in Fig. 1, we acquired 543 views (30 cm \times 40 cm field of view) over 20 s at the four voltages and four detector entrance dose request settings. The associated tube currents (mAs per view) were recorded in order to rescale the standard CTDI head phantom dose data to the CATPHAN based on the mAs ratio. When the CATPHAN was scanned at 70 kVp with the detector entrance dose request set to a high level, the voltage increased beyond 70 kVp to reach the specified detector input exposure. This data set was not included in the study.

Scaling of the CTDI 16 cm phantom dose data to obtain a realistic estimate of dose to the CATPHAN deviates from the normal methodology used with an “index” dose. The normal procedure in conventional, narrow-beam CT has been to report only the index doses (CTDI) in the standard dosimetry phantoms, but to use the same manual technique (kVp, mAs) on both the low-contrast performance and dosimetry phantoms. In our case, we are under AEC control, such that it is not possible to use the same mAs technique on both phantoms.

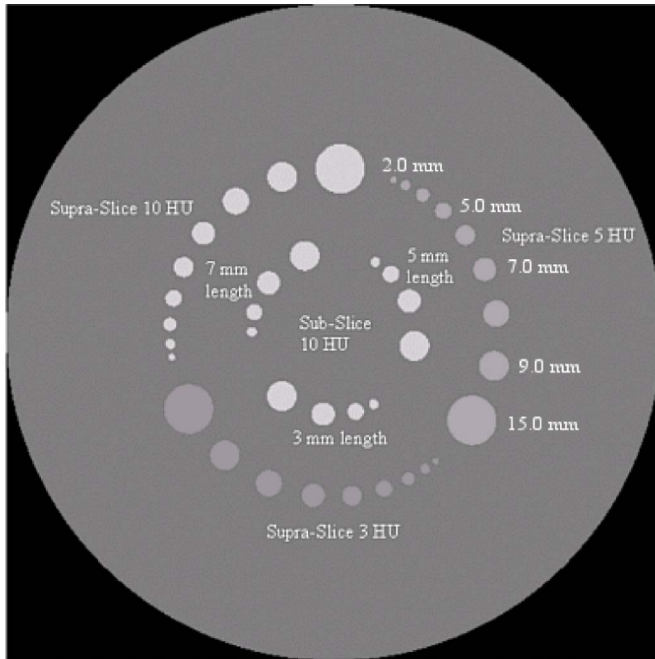


FIG. 2. CATPHAN CTP515 low contrast module with low-contrast targets. The nominal contrast levels of the nine outer supra-slice targets are 0.3%, 0.5%, and 1.0%. Their diameters range from 2.0 mm to 9.0 mm in 1 mm steps, and a 15 mm target completes each contrast group.

After two-dimensional image acquisition, projection images were sent to a workstation (XLeonardo P15, Siemens Medical Solutions, Forchheim, Germany), and sixteen 3D data sets were generated (four tube voltages, four entrance dose request settings). A modified Feldkamp algorithm was used for image reconstruction taking the noncircular but reproducible C-arm imaging geometry²² into account using projection matrices.^{23,24} It involves properly adjusted cosine weighting of the normalized input projection data, a one-dimensional convolution with a shift-invariant kernel, and a weighted cone-beam back-projection step. In addition, beam hardening and scatter corrections were applied as discussed in Ref. 25. The kernel used for reconstruction was system standard, a modified Shep-Logan filter with a roll-off starting at 18% of the Nyquist frequency. The frequency response decreases to 10% of its maximum value at approximately half the Nyquist frequency. Voxels were reconstructed with a size of 0.85 mm, and a slice width of 10 mm was selected for display. The display window center was adjusted such that its center value coincided with the mean background value for each image. The display window width was fixed at 100 gray levels.

Each observer read the 16 images on a single soft-copy monitor under controlled viewing conditions in a single session to keep intraviewer variability small. The observer experience ranged from inexperienced (graduate students) to experienced (image quality experts). All image identification was removed so observers were unaware of the underlying imaging parameters. Only targets at the 0.5% nominal contrast level were scored. Observers were asked to determine the smallest (nominal) 0.5% object visible to them. There

were five observers and a total of 13 sessions (most observers participated in two sessions, separated in time by a minimum of two weeks; one observer read the images four times) yielding a total of 208 scored images. The frequency of target detection was recorded using detectability profiles. They list how often a 0.5% nominal contrast object with a particular size was seen. For example, if the 10 mm object contrast was seen in ten out of 13 observations, then 77% detectability was assigned. These results resemble the true positive fraction of a receiver-operating study. Detectability was measured by investigating the size at which the detectability chart crossed certain specific thresholds; e.g., the 50% or 100% level.

System MTF was measured using one set of the imaging parameters from above. Projections were acquired at 70 kVp, and reconstructed into a 512×512 grid using a voxel size of 0.02 mm (FOV 1.024 cm). Volumes were reconstructed using the same kernel as for the detectability study ("smooth") and for two other kernels that provide less smoothing while using the same acquisition frame rate and matrix (a pure Shepp-Logan filter provided highest resolution). To calculate the MTF from the slice images, profiles in one direction in 205 reconstructed slices down the length of the wire were first aligned using the maximum value in each profile and then averaged together to improve noise characteristics of the profile. Alignment was necessary since exact positioning of the wire with respect to the detector axis is difficult for a C-arm system with noncircular geometry. This approach provides an oversampled estimate of the system point spread function.²⁶ A fit to the tails was used to remove the offset, and after deconvolution of the wire diameter from the function, the Fast Fourier transform normalized to zero spatial frequency provided the MTF.

C. Dose efficiency analysis

The visibility of an object reconstructed from x-ray projections depends on the incident dose at the detector of the associated views and the tube voltage.²⁷ To compare detectability profiles obtained for different dose settings, they can be normalized to a common reference dose based on an "equivalent diameter" d_{ref} described below.

To derive a suitable relationship between detectability profiles obtained at different dose levels but identical tube voltage, recall that Rose's definition for a threshold signal-to-noise ratio (SNR) can be rewritten based on signal detection theory²⁸ as

$$\text{SNR} = \frac{a\sqrt{A}}{\sigma}. \quad (2)$$

In this equation, a represents the signal level or contrast in this case, σ is the standard deviation of the noise, and A is the signal area. For quantum noise-limited CT systems, noise is inversely proportional to the square root of the dose to the detector.²⁹ Since $\bar{D}(0)$ as measured for the 16 cm CTDI phantom turns out to be proportional to incident detector

dose at a fixed kVp as well (see Fig. 4 below), image noise is also inversely proportional to $\sqrt{\bar{D}(0)}$; i.e.,

$$\sigma \propto \frac{1}{\sqrt{\bar{D}(0)}}. \quad (3)$$

If we combine both equations and further assume circular objects with diameter d and area $A=(d/2)^2\pi$, we get

$$\text{SNR} \propto a \frac{d}{2} \sqrt{\pi} \sqrt{\bar{D}(0)}. \quad (4)$$

Assuming a fixed threshold SNR and constant signal amplitude a at a fixed tube voltage, we arrive at a relationship between the diameters of just visible objects and their associated dose values:

$$d_1 \cdot \sqrt{\bar{D}_1(0)} = d_2 \cdot \sqrt{\bar{D}_2(0)}. \quad (5)$$

For objects with identical contrast (same a), this equation answers the question of which diameter (d_2) could be seen if the dose were changed from $\bar{D}_1(0)$ to $\bar{D}_2(0)$.

By rearranging Eq. (5), we can find a simple mechanism to normalize detectability charts to a common reference dose. We get a new diameter d_{ref} of the just visible object at the reference dose $\bar{D}_{\text{ref}}(0)$, as

$$d_{\text{ref}} = \sqrt{\frac{\bar{D}(0)}{\bar{D}_{\text{ref}}(0)}} \cdot d. \quad (6)$$

Equation (6) appears very useful for a dose-based analysis of 3D C-arm imaging results, because C-arm x-ray devices often have a built-in automatic exposure control making it difficult to specify scan doses *a priori*. Interestingly, Eq. (6) has previously been proposed without derivation in a paper by Ishida *et al.*, in which they demonstrated its utility in converting various dose-dependent detectability profiles into a common chart.¹⁹ Their goal was to derive a Dose Efficiency Index, defined as the target contrast and diameter that can be detected visually with 50% probability at the reference dose.

Since Eq. (6) is based on the threshold SNR for object detection within a uniform noisy background, it no longer applies exactly if there are other artifacts impairing image quality (beyond noise), nor does it account for differing observer-dependent S/N thresholds. While the equation cannot be expected to always yield exact results, we still found it to be very helpful as an approximation to simplify and facilitate comparisons, such as the impact of x-ray tube voltage on the low-contrast imaging performance of a 3D C-arm device. To this end, we transformed all detectability profiles to a common reference dose by rescaling their abscissas (diameters) using Eq. (6). We then calculated the mean detectability curve for each kVp by averaging the adjusted detectability profiles at each normalized diameter. Finally, we compared the mean detectability profiles associated with the reference dose at various kVps and analyzed their differences.

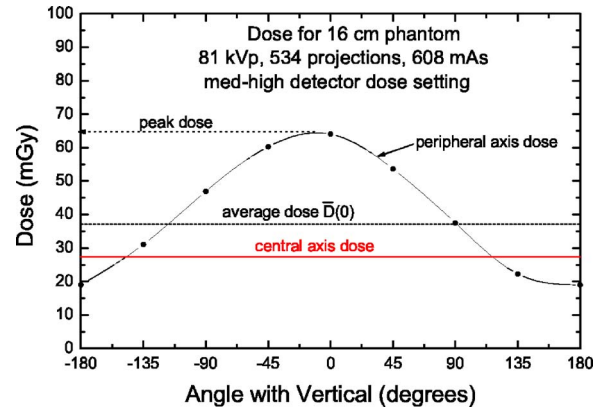


FIG. 3. Dose in 16 cm Perspex phantom at various peripheral axis points at 1 cm depth around the phantom circumference. Also indicated is the central axis dose value and the average dose $\bar{D}(0)$ in the central plane computed using Eq. (1).

III. RESULTS

We first present dose measurements for the standard 16 cm Perspex® phantom for a range of tube voltages and detector dose settings. We then present detectability profiles for the 0.5% contrast objects, and finally compare average detectability profiles for different kVp settings. An examination of the normalized detectability profiles provides some guidance for optimum choice of kVp, at least for objects having diameters and composition similar to those studied here.

A. Dose measurements

Figure 3 shows a plot of the peripheral axis dose at $r=7$ cm in the central plane ($z=0$) of the 16 cm diameter phantom versus its angular offset from the vertical, where $\theta=0$ represents the beam central ray directed vertically upward, measured for a 543 view, 20 s acquisition at 81 kVp, for a “medium-high” detector dose setting (0.46 $\mu\text{Gy}/\text{view}$), which demanded a total of 608 mAs.

Also shown is the central axis dose ($r=0$), the peak entrance dose at $\theta \approx 0$, and the average dose over the central plane $\bar{D}(0)$ given by Eq. (1). The slight apparent asymmetry is due to the asymmetry of the scan trajectory about $\theta=0$ such that the real symmetry axis in Fig. 3 is at -9.5° . The relative peripheral-to-central-axis dose *ratio* [and thus $\bar{D}(0)$ as well] is independent of detector dose demand setting, and depends only weakly on kVp, with the peak-to-central-axis ratio varying from 2.5 at 70 kVp to 2.0 at 125 kVp. The ratio of $\bar{D}(0)$ to the peak dose varies by only 6% (from 0.57 to 0.61) over the entire kVp range of 70–125 kVp, thus, the metric $\bar{D}(0)$ is also indicative of the peak dose.

Figure 4 illustrates the linearity of phantom dose with detector dose demand, as illustrated by the linear regression fits.

The ratio of $\bar{D}(0)$ to the peak and central axis doses versus detector dose is constant as expected (to within $\pm 1\%$, indi-

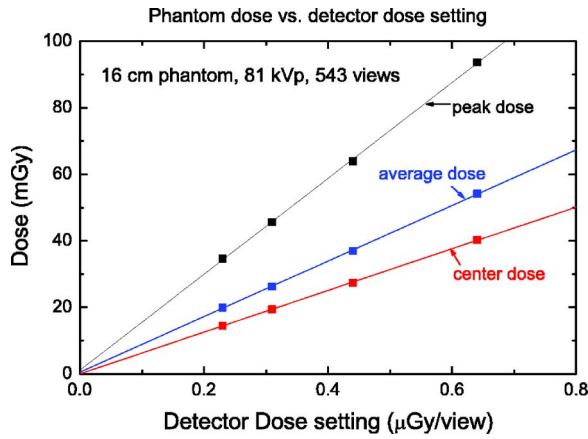


FIG. 4. Phantom dose versus detector dose demand, with linear regression fits. Average dose is $\bar{D}(0)$.

cating excellent measurement consistency), the ratios being equal to 0.58 and 1.36, respectively, at 81 kVp.

The purpose of these dose determinations is to label each image used in the following image quality evaluations with a relevant and representative dose metric, viz., the average dose across the central plane at $z=0$, which we have denoted as $\bar{D}(0)$, in order to provide a familiar reference frame for comparison with conventional CT dose, such as with $CTDI_w$.

The “water-equivalent” diameter of the 16 cm Perspex® phantom ($\rho=1.2 \text{ g cm}^{-3}$) is approximately 19 cm, which is only slightly less than the 20 cm diameter CATPHAN (inside of which no dose measurement is possible). Recall that we took the somewhat unorthodox step of scaling the measured 16 cm dosimetry phantom dose values to estimated doses in the CATPHAN, and the images presented are “tagged” with the scaled $\bar{D}(0)$. These values are shown in Table II for the

TABLE II. Resulting phantom dose values for medium-high detector entrance dose request. (a) $\bar{D}(0)$ for 16 cm CTDI Phantom (543 Views). Medium-high detector dose demand setting. (b) CATPHAN dose: scaled (by mAs ratio) from the measured 16 cm CTDI phantom dose.

(a)					
kVp	Total mAs	Detector dose (uGy/view)	Peak dose (mGy)	Center dose (mGy)	$\bar{D}(0)$ (mGy)
70	1167	0.46	85.7	33.9	48.4
81	608	0.44	63.5	27.4	37.0
109	310	0.70	65.5	31.5	39.6
125	260	0.92	75.6	37.6	46.0
(b)					
kVp	Total mAs	Detector dose (uGy/view)	Peak dose (mGy)	Center dose (mGy)	$\bar{D}(0)$ (mGy)
70	1676	0.46	123.1	48.7	69.4
81	907	0.44	94.7	40.8	55.2
109	392	0.70	82.9	39.8	50.1
125	299	0.92	87.0	43.3	52.9

TABLE III. Nominal contrast percent as specified by the CATPHAN manufacturer compared to measured contrast values $C\%$ using the observed HU differences. As expected, the contrast decreased with increasing kVp.

Nominal contrast specified by manufacturer	1%	0.5%	0.3%
Measured at 70 kVp	1.22	0.49	0.36
Measured at 81 kVp	1.18	0.47	0.35
Measured at 109 kVp	1.04	0.43	0.37
Measured at 125 kVp	0.97	0.36	0.34

“medium-high” detector demand setting. While the doses in the two phantoms differ by only 15% at 125 kVp, the CATPHAN demands 50% more mAs and dose at 70 kVp.

Note that for the medium-high AEC setting, the measured detector entrance dose ($\mu\text{Gy/view}$) does not remain constant, thus producing the increase in phantom dose observed at higher kVp. This dose increase is due to the AEC optimization software, which uses a complicated manufacturer-designed algorithm to change mAs (and sometimes kVp) depending on the requested dose and kVp. The 16 cm phantom results indicate that the medium-high dose for C-arm CT head scans for 543 views taken over 20 s results in an average dose of 40–48 mGy.

B. Image quality assessment

The true contrast of the CATPHAN phantom was verified by measuring the mean signal in the largest 15 mm object for the highest dose acquisition and in an equal area in the background. Care was taken to ensure that signal and background were measured at the same radius, so that any residual beam hardening and scatter effects after correction were somewhat reduced in the measurements. The results are summarized in Table III and indicate a small decrease in phantom contrast with increasing kVp as expected.

Figure 5(a) shows a full image of the CATPHAN phantom (81.7 mGy, 81 kVp) as an example of the images presented to the observers for the detectability study. Figures 5(b)–5(e) show the 5 HU contrast circles of Fig. 5(a) for slices from four volumes also acquired at 81 kV but at different doses. The window and level are the same as those used for the detectability study, with the window level equal to the mean of the background, and the window width set to 100 HU. Both noise and ring artifacts decrease with increasing dose, since the ring artifact correction algorithm performs better under low-noise (higher dose) conditions.

Figure 6 shows the detectability curves corresponding to the images of Fig. 5 at 81 kVp. The dotted curve at the lowest detector dose corresponding to the image in Fig. 5(b) shows that the 10 mm insert was seen in only about 40% of all observations. Even the 15 mm insert was visible in only 46% of all experiments. The dashed curve (corresponding to

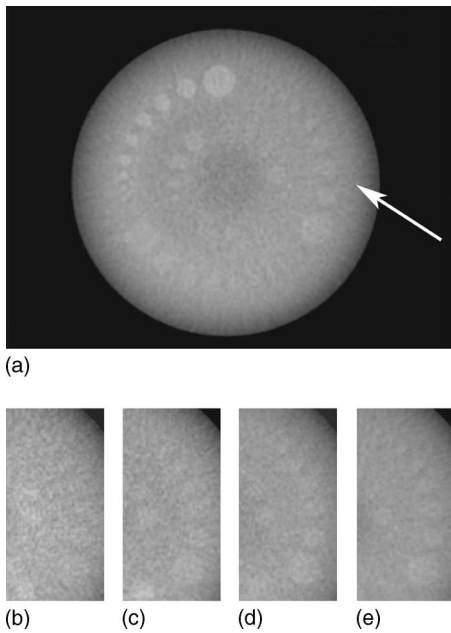


FIG. 5. CATPHAN slice section reconstructed from projections acquired at 81 kVp. (a) full slice at highest dose setting of 81.7 mGy and subregions of slices at (b) 27.3 mGy, (c) 38.4 mGy, (d) 56.6 mGy, and (e) 81.7 mGy. These are rescaled dose values based on the mAs applied during CATPHAN scanning with respect to the mAs used to for the dosimetry head phantom (at the same tube voltage).

the image in Fig. 5(e)), on the other hand, shows that 5 mm diameter objects could be detected in 76% of all readings at the highest dose setting. As expected, the higher the dose, the smaller the diameter of a just-visible object.

C. MTF measurement

The measured MTFs are shown in Fig. 7 for three different kernels, with the “smooth” curve corresponding to that used for the detectability study. Even with the smooth kernel,

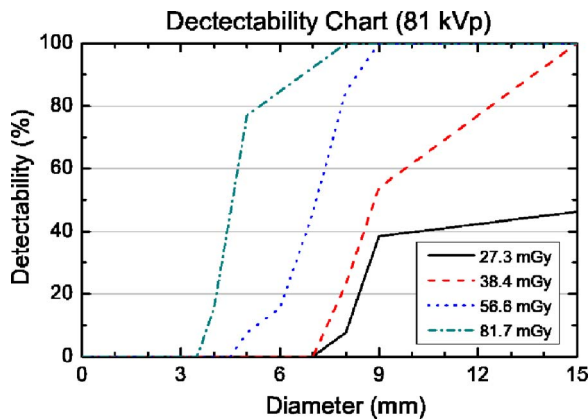


FIG. 6. 81 kVp detectability profiles associated with the slice sections shown in Fig. 5. The 27.3 mGy curve indicates that the 15 mm diameter object might just be visible (based on a 50% detectability threshold), the 38.4 mGy curve suggests that you should see objects larger than 9 mm, the 56.6 mGy curve implies a minimum size of 7 mm, and the 81.7 mGy curve hints at detectability of insets with smallest diameter between 4 and 5 mm. These results agree reasonably well with a visual inspection of Fig. 5.

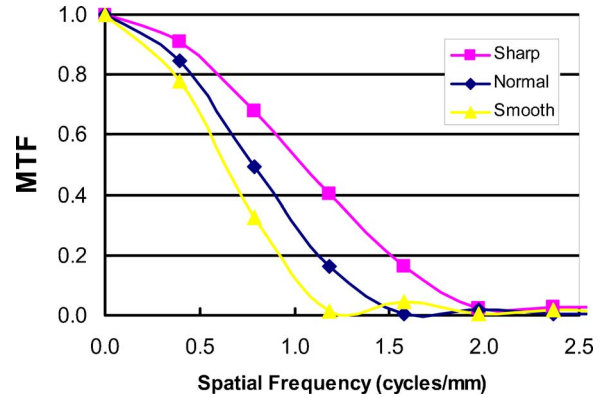


FIG. 7. Modulation transfer function of a 100 μm wire in a volume reconstructed using the same kernel as was used for the detectability studies, and for two other kernels illustrating potential system resolution when operated in a similar mode.

the system has a 10% MTF at 0.5 mm, and has been shown in other studies to be isotropic. We expect that the choice of this kernel provided some noise reduction, and since the detectability study was carried out using thick (1 cm) multiplanar reformatted slices, the reduction in resolution was considered to be acceptable.

D. Dose-efficiency analysis

Figure 8 shows three detectability curves acquired at 81 kVp, and normalized to the same dose by applying Eq. (6). While the curves of Fig. 8 moved closer together, the congruence is not perfect. An average curve, corresponding to the same dose, was computed by averaging three detectability numbers at each normalized diameter. Note that the lowest dose curve corresponding to Fig. 5(b) was not used, since Eq. (6) assumes a stationary noise background and the presence of significant ring artifact in Fig. 5(b) did not meet this criterion.

The same approach was applied to arrive at the three average normalized detectability curves for 70, 109, and

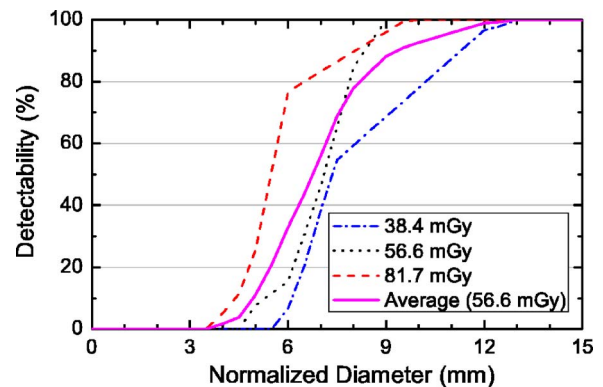


FIG. 8. Normalized detectability charts for objects reconstructed from 81 kVp projections at different dose levels. The detectability chart diameters formerly associated with 38.4 and 81.7 mGy have been normalized to 56.6 mGy using Eq. (6).

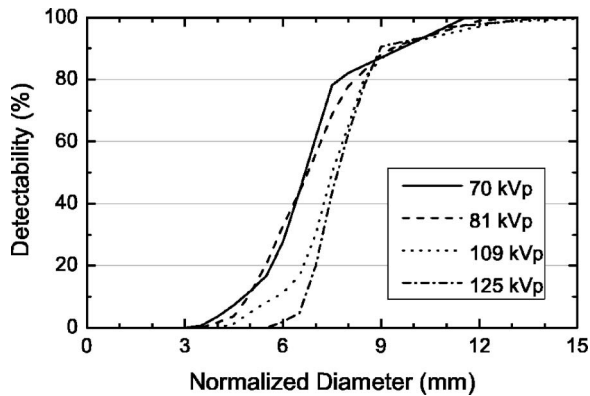


FIG. 9. Average normalized detectability charts at 70, 81, 109, and 125 kVp. The object diameters have been normalized to 56.6 mGy using Eq. (6).

125 kVp shown in Fig. 9, where all average curves have been normalized to the same reference dose of 56.6 mGy.

At 56.6 mGy, larger objects ($d > 9$ mm) with nominal contrast difference of 0.5% are generally visible from 70 kVp through 125 kVp. At higher tube voltages, the loss of object contrast moves the detectability curves to the right.

An illustration of the effect of increased contrast at lower dose is shown in Fig. 10. The contrast appears to be higher on the left, i.e., for lower tube voltage, but there is also more noise. More image noise at lower tube voltage is expected, because at lower kVp you have to request a lower detector entrance dose to arrive at a similar average object dose $\bar{D}(0)$ compared to higher tube voltages. The 9 and 15 mm test objects are visible in all cases, but the smaller objects are better visualized at lower tube voltages.

IV. DISCUSSION

This study indicates that for an Axiom Artis dTA (VB22D) system equipped with a Trixell Pixium 4700 detector, improved 3D imaging performance for small, low-contrast objects at a fixed dose is obtained for lower tube voltages. Larger objects could be seen equally well at the kVps investigated. Since this result was obtained for the detectability of low atomic number materials, we can expect a larger performance difference for high atomic number materials, e.g., for studies involving iodine.^{30,31} From this we conclude that one should preferably operate at 70 kVp in particular for studies involving small vessels filled with

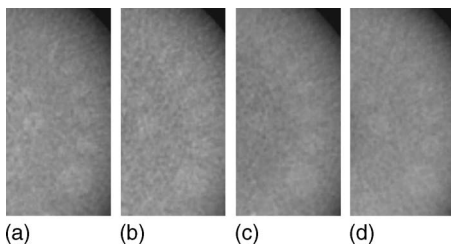


FIG. 10. Reconstructed CATPHAN sections at comparable $\bar{D}(0)$ dose levels (indicated in parentheses) but at (a) 70 kVp (49.8 mGy), (b) 81 kVp (56.6 mGy), (c) 109 kVp (51.9 mGy), and (d) 125 kVp (56.6 mGy).

iodine—at least as long as there are no other dominating artifacts, e.g., due to beam hardening or photon starvation and assuming that the dose administered to the patient is acceptable. Increasing the tube voltage, on the other hand, is unlikely to dramatically reduce the low-contrast image quality, and it will be beneficial to reduce the patient dose when scanning larger objects.

In general, C-arm systems such as the one used for this study are optimized for visualization of small, iodine-filled vessels, and the ratio of $\text{SNR}^2/(\text{entrance exposure})$ for a flat-panel-based cone-beam system was previously shown to decrease with increasing kVp.³² The beam quality is significantly softer than is typically used for clinical CT image acquisition, and detector parameters, such as thickness of the CsI conversion layer, is also optimized for this beam quality. It is therefore not surprising that better performance occurs at lower kVps. Note, however, that this conclusion applies only to smaller-diameter anatomical structures such as the head; in *in vivo* head scans the presence of the high-Z skull may alter these results somewhat (the CATPHAN did not have a skull simulating annulus). When imaging larger diameter objects such as the chest or abdomen, tube output limitations may push kVp up in order to ensure that the detector continues to operate in the quantum-noise-limited regime and that the correction algorithms (such as that for ring artifact) perform well. In addition, artifacts such as those due to beam hardening, which were not a significant problem in this low-contrast study, may dictate use of higher kVp. Further optimization of beam filtration in a study that includes noise and artifact level is still necessary.

Our 16 cm phantom dose results indicate that the medium or medium-high detector dose setting for C-arm CT (Dyna CT, Siemens Medical Solutions) for head scans using 543 views taken over 20 s is close to the EU guideline³³ and the ACR reference value³⁴ for conventional CT head scans of 60 mGy. Traditionally, views for 3D angiographic applications (vessel trees) are acquired over 5 or 10 seconds. In this case, the dose would be about a factor of four or two lower than the EU or ACR guidelines although detectability of small, low-contrast objects would, of course, decrease as the SNR decreased.

The low contrast detectability of currently used conventional CT scanners depends on the exposure and image reconstruction parameters used, but one can expect to reliably see the 0.3% nominal contrast objects of size 5 mm [1.5% mm] at 125 kVp in the CATPHAN 600 using dose and visualization settings comparable to ours.³⁵ Figure 9 shows that the Artis dTA system used for this image quality study can generally resolve 0.5% nominal contrast objects with a minimum size of 9 mm [4.5% mm] for a dose setting that is comparable to that used in clinical CT. More precisely, all observers saw at least the 9 mm object with nominal contrast of 0.5% at 70, 81, and 109 kVp. At 125 kVp, only the 15 mm object had 100% detectability, but the 9 mm object was still seen in 92% of all readings.

While the low-contrast detectability does not match that of clinical CT, the C-arm system was shown to provide image

quality that is clinically useful during intracranial interventional procedures.⁹ For such procedures, the ability to detect a fresh intracranial bleed in the absence of contrast is particularly useful since the presence of a fresh bleed may significantly change the course of the treatment. Detecting a fresh bleed requires resolving a signal difference of ~ 40 HU. Our results indicate that this is possible. However, the presence of additional artifacts may considerably complicate this imaging task. It should also be noted that the low contrast objects in CATPHAN used for this study are manufactured primarily by altering mass density, whereas, in clinical use of C-arm CT one is often observing low contrast objects produced by the higher atomic number of dilute contrast agents, hence the lower kVp and beam quality of C-arm CT may provide an advantage over conventional CT in this arena. It is therefore of interest to also study low contrast perceptibility with iodinated low-contrast test objects (such as used in some DSA phantoms).

In our detectability study, we scaled the dose measured in the 16-cm perspex phantom using mAs to represent dose in the CATPHAN and then labeled the images in the detectability study using this scaled dose value. We chose this approach since the current implementation of C-arm CT uses the AEC system to modify exposure as the C-arm rotates around the subject, and mAs cannot be fixed. In fact, use of AEC is analogous to mA modulation in CT, which is preferred for noise uniformity and dose reasons.^{21,36} It is clear that the observed low-contrast detectability in the CATPHAN is more closely related to its own mAs demand and dose deposited therein, rather than to the mAs demand and dose in the 16 cm Perspex® phantom, therefore this scaling method has the same effect as performing the dose phantom measurement at the same mAs as that used with the performance phantom. This of course begs the question as to which better represents the patient dose in a clinical head scan. In addition, the fact that the mAs used differs by 50% at low kVp leads one to speculate that a Perspex phantom may not be the most appropriate choice for the “softer” beam quality of C-arm CT (Table I), with a water phantom, solid water, or other tissue-equivalent materials being better choices. Thus both of our old “CTDI” tools (pencil chamber and Perspex phantoms) are questionable in the arena of cone-beam CT.

The dosimetry phantom length (14 cm) was approximately 2/3 of the beam width at the center of rotation. However, we took point dose measurements in the central phantom plane and not an integral measurement, and it is unlikely that adding additional scatter volume beyond ± 7 cm increases the central plane dose by a large amount in the head phantom and, of course, the length of an actual head is finite. In addition, the length of the dosimetry phantom is somewhat comparable to the CATPHAN 600 length. Nevertheless, a longer dosimetry phantom is preferable for dose measurements—both for C-Arm CT and for conventional CT. Note that for the same central dose, the dose-length-products for C-arm and conventional CT would not be expected to be too dissimilar. This will be the subject of future work.

V. CONCLUSIONS

The results presented here are intended to serve two purposes. First, we have outlined a dose metric and measurement technique with application to wide cone-beam CT systems such as C-Arm CT as well as to other more conventional cone beam CT systems using flat panel detectors having wide x-ray beams (along the z axis). Our definition of $\bar{D}(0)$ can be used to benchmark such systems against conventional narrow-beam clinical CT systems by comparing it to CTDI_w . Second, a perception study involving the CATPHAN 600 showed that one can expect to see at least the 9 mm inset with 0.5% nominal contrast at the recommended head-scan dose level (60 mGy) when using tube voltages ranging from 70 to 125 kVp. Third, we have shown that for C-arm systems optimized for angiographic applications, use of a lower kVp for CT imaging provides improved image quality for small low-contrast inserts in head-sized objects. Further investigation is required to expand this study to larger-diameter objects. The 32 cm diameter Perspex® CTDI body phantom represents a very large patient (having a 100 cm circumference or 48 in waist size when scaled to unit density), and may not be the best choice.

ACKNOWLEDGMENTS

The authors wish to acknowledge the expert technical assistance of Nicolas Mervin, Philipp Bernhardt, Thomas Brunner and N. Robert Bennett. This research was supported by NIH R01EB003524, The Lucas Foundation, and Siemens Medical Solutions.

- ¹U. Missler, C. Hundt, M. Wiesmann, T. Mayer, and H. Brackmann, “Three-dimensional reconstructed rotational digital subtraction angiography in planning treatment of intracranial aneurysms,” *Eur. Radiol.* **4**, 564–568 (2000).
- ²A. Hochmuth, U. Spetzger, and M. Schumacher, “Comparison of three-dimensional rotational angiography with digital subtraction angiography in the assessment of ruptured cerebral aneurysms,” *AJNR Am. J. Neuroradiol.* **23**, 1199–1205 (2002).
- ³J. K. Song, Y. Niimi, J. L. Brisman, and A. Berenstein, “Simultaneous bilateral internal carotid artery 3D rotational angiography,” *AJNR Am. J. Neuroradiol.* **25**, 1787–1789 (2004).
- ⁴D. A. Jaffray, J. H. Siewerdsen, and D. G. Drake, “Performance of a volumetric CT scanner based upon a flat-panel imager,” *Proc. SPIE* **3659**, 204–214 (1999).
- ⁵D. A. Jaffray and J. H. Siewerdsen, “Volumetric cone-beam CT system based on a 41×41 cm² flat-panel imager,” *Proc. SPIE* **4320**, 800–807 (2001).
- ⁶G. Rose, J. Wiegert, D. Schaefer, K. Fiedler, N. Conrads, J. Timmer, V. Rasche, N. Noordhoek, E. Klotz, and R. Koppe, “Image quality of flat-panel cone beam CT,” *Proc. SPIE* **5030**, 677–684 (2003).
- ⁷J. Wiegert, M. Bertram, D. Schaefer, N. Conrads, N. Noordhoek, K. de Jong, T. Aach, and G. Rose, “Soft-tissue contrast resolution within the head of human cadaver by means of flat-detector-based cone-beam CT,” *Proc. SPIE* **5368**, 330–337 (2004).
- ⁸R. Fahrig, A. Ganguly, J. D. Starman, and N. K. Strobel, “C-arm CT with XRIIs and digital flat panels: a review,” *Proc. SPIE* **5535**, 400–410 (2004).
- ⁹H. Arakawa, M. P. Marks, H. M. Do, N. Strobel, and R. Fahrig, “Experimental study of intracranial hematoma detection with flat panel detector C-arm CT,” Joint Annual Meeting of the AANS/CNS Cerebrovascular Section and The American Society of Interventional & Therapeutic Neuroradiology, Orlando, Florida, 2006, p. 71.

- ¹⁰D. L. Miller *et al.*, "Radiation doses in interventional radiology procedures: The RAD-IR study: Part I: Overall measures of dose," *J. Vasc. Interv Radiol.* **14**, 711–722 (2003).
- ¹¹D. L. Miller *et al.*, "Radiation doses in interventional radiology procedures: The RAD-IR study: Part II: Skin Dose," *J. Vasc. Interv Radiol.* **14**, 977–990 (2003).
- ¹²S. Balter *et al.*, "Radiation doses in interventional radiology procedures: The RAD-IR study: Part III: Dosimetric performance of the interventional fluoroscopy units," *J. Vasc. Interv Radiol.* **15**, 919–926 (2004).
- ¹³B. A. Schueler, D. F. Kallmes, and H. J. Cloft, "3D cerebral angiography: Radiation dose comparison with digital subtraction angiography," *AJNR Am. J. Neuroradiol.* **26**, 1898–1901 (2005).
- ¹⁴J. N. Kroon, "3-Dimensional rotational X-ray imaging, 3D-RX: image quality and patient dose simulation for optimisation studies," *Radiat. Prot. Dosim.* **114**, 341–349 (2005).
- ¹⁵R. Fahrig, R. Dixon, J. T. Payne, R. Morin, A. Ganguly, and N. Strobel, "Characterization of dose distribution and image quality in 3D volume images reconstructed from data acquired on a flat-panel-based C-arm angiography system." *RSNA, SSC16–09, Chicago (RSNA, Oak Brook, IL, 2005).*
- ¹⁶R. L. Dixon, "A new look at CT dose measurement: Beyond CTDI," *Med. Phys.* **30**, 1272–1280 (2003).
- ¹⁷J. A. Anderson, T. Dallas, D. P. Chason, T. J. Lane, and A. L. McAnulty, "CT dosimetry and the new modalities: Cone-beam and wide area CT," *RSNA 2004, Chicago (RSNA, Oak Brook, IL, 2004)*, p. 735.
- ¹⁸C. Suess, W. A. Kalender, and J. M. Coman, "New low-contrast resolution phantoms for computed tomography," *Med. Phys.* **26**, 296–302 (1999).
- ¹⁹T. Ishida, S. Tsukagoshi, K. Kondo, K. Kainuma, M. Okumura, and T. Sasaki, "Evaluation of dose efficiency index compared to receiver operating characteristics for assessing CT low-contrast performance," *Proc. SPIE* **5368**, 527–533 (2004).
- ²⁰M. Spahn, "Flat detectors and their clinical applications," *Eur. Radiol.* **15**, 1934–1947 (2005).
- ²¹M. Gies, W. A. Kalender, H. Wolf, C. Suess, and M. T. Madsen, "Dose reduction in CT by anatomically adapted tube current modulation. I. Simulation studies," *Med. Phys.* **26**, 2235–2247 (1999).
- ²²R. Fahrig and D. W. Holdsworth, "Three-dimensional computed tomographic reconstruction using a C-arm mounted XRRI: image-based correction of gantry motion nonidealities," *Med. Phys.* **27**, 30–38 (2000).
- ²³L. A. Feldkamp, L. C. Davis, and J. W. Kress, "Practical cone-beam algorithm," *J. Opt. Soc. Am.* **1**, 612–619 (1984).
- ²⁴K. Wiesent, K. Barth, N. Navab, P. Durlak, T. Brunner, O. Schuetz, and W. Seissler, "Enhanced 3-D-reconstruction algorithm for C-arm systems suitable for interventional procedures," *IEEE Trans. Med. Imaging* **19**, 391–403 (2000).
- ²⁵M. Zellerhoff, B. Scholz, E. P. Ruehrschopf, and T. Brunner, "Low contrast 3D reconstruction from C-arm data," *Proc. SPIE* **5745**, 646–655 (2005).
- ²⁶E. L. Nickoloff, "Measurement of the PSF for a CT scanner: appropriate wire diameter and pixel size," *Phys. Med. Biol.* **33**, 149–155 (1988).
- ²⁷K. M. Hanson, "Noise and contrast discrimination in computed tomography," in: *Technical Aspects of Computed Tomography* Vol. 5, edited by D. G. Newton THaP (C.V. Mosby, St. Louis, 1981).
- ²⁸A. E. Burgess, "The Rose model, revisited," *J. Opt. Soc. Am.* **16**, 633–646 (1999).
- ²⁹G. Brooks RAaDC, "Statistical limitations in x-ray reconstructive tomography," *Med. Phys.* **3**, 230–237 (1976).
- ³⁰W. Huda, K. A. Lieberman, J. Chang, and M. L. Roskopf, "Patient size and x-ray technique factors in head computed tomography examinations. II. Image quality," *Med. Phys.* **31**, 595–601 (2004).
- ³¹M. A. Staniszewska, M. Obrzut, and K. Rybka, "Phantom studies for possible dose reduction in CT head procedures," *Radiat. Prot. Dosim.* **114**, 326–331 (2005).
- ³²R. Ning, B. Chen, R. Yu, D. Conover, X. Tang, and Y. Ning, "Flat panel detector-based cone-beam volume CT angiography imaging: system evaluation," *IEEE Trans. Med. Imaging* **19**, 949–963 (2000).
- ³³European Commission, "Quality criteria for computed tomography: working document," Publication EUR 16262 (European Commission, Brussels, Belgium, 1997).
- ³⁴J. E. Gray, B. R. Archer, P. F. Butler, B. B. Hobbs, F. A. Mettler, Jr., R. J. Pizzutiello, Jr., B. A. Schueler, K. J. Strauss, O. H. Suleiman, and M. J. Yaffe, "The American Association of Physicists in Medicine Task Group on Reference Values for Diagnostic XrE. Reference values for diagnostic radiology: application and impact," *Radiology* **235**, 354–358 (2005).
- ³⁵D. Platten, N. Keat, M. Lewis, J. Barrett, and S. Edyvean, "Siemens Sensation 16 CT Scanner Technical Evaluation," Evaluation Report 04037: ImPACT-MHRA, 2004.
- ³⁶W. A. Kalender, H. Wolf, and C. Suess, "Dose reduction in CT by anatomically adapted tube current modulation. II. Phantom measurements," *Med. Phys.* **26**, 2248–2253 (1999).